TRANSPORT OF HIGH BOILING POINT FIRE SUPPRESSANTS IN A DROPLET-LADEN HOMOGENEOUS TURBULENT FLOW PAST A CYLINDER

C. Presser*

Chemical Science and Technology Laboratory, National Institute of Standards and Technology, Gaithersburg, MD 20899-8360, USA

C. T. Avedisian

Sibley School of Mechanical and Aerospace Engineering, Cornell University, Ithaca, NY 14853-7501, USA

Liquid agent transport was investigated around unheated and heated horizontal cylinders (to a near–surface temperature of approximately 423 K, i.e., well above the water boiling point) under ambient conditions. Experimental results are presented for a well-characterized, droplet-laden homogenous turbulent flow field, using water, methoxy–nonafluorobutane (i.e., HFE-7100, $C_4F_9OCH_3$, with a boiling point of 334 K), and 1-methoxyheptafluoropropane (i.e., HFE-7000, $C_3F_7OCH_3$, with a boiling point of 307 K). Phase Doppler interferometry and visualization techniques were used to explore the thermal effects on spray surface impingement, vaporization, and transport around and downstream behind the cylinder by providing information on droplet size and velocity in the vicinity of the cylinder. For water, results indicated that impinging droplets larger than about 35 μm generally coat the unheated cylinder surface, with few droplets rebounding back into the free stream. Downstream, in the wake region of the cylinder, smaller size droplets (generally, of less than 35 μm) are entrained into the recirculation zone. Heat transfer reduces droplet mean size and velocity significantly in the vicinity of the heated cylinder. For the two HFE agents, liquid coating and dripping (observed for water) were eliminated due to vaporization. Droplet mean size increases and velocity decreases with increasing agent boiling point. These variations may also be explained by the changes in agent physical properties. It is improbable that shattering occurs for the droplet sizes and velocities encountered for the given operating conditions, although it could conceivably occur for a few individual impinging droplets.

INTRODUCTION

Fires within an aircraft engine nacelle pose a significant hazard for suppression owing to the presence of wires, fuel, hydraulic and electrical lines, ribs, and other objects (e.g., mounting brackets) which can obstruct transport of a suppression agent to the source (e.g., broken fuel line). Non-ozone-depleting halogen alternatives developed for such applications include chemical suppressants that have high boiling point temperatures ($T_b > 330$ K) and exist in the liquid phase under high-pressure release or in ambient conditions. Liquid suppressants are of interest because of their higher absorption of heat per unit volume compared to gaseous suppressants, which results in a greater reduction of flame and surface temperatures [1]. Release of these agents in a confined, cluttered space results in the dispersal of droplets that may impact on solid surfaces and reduce the fire suppression effectiveness of the agent.

The complex arrangement of components inside an aircraft engine nacelle creates an environment for spray transport that is characterized by a high degree of turbulence, high blockage ratios, and significant liquid impingement onto surfaces. We examined aspects of this complex dynamic from the simplified perspective of droplet-laden flow past a single cylinder to provide benchmark data for fire suppression model validation. Droplet size and velocity were obtained for a spray directed at a horizontal

---

627

cylinder (oriented normal to the airstream and spray) in a grid-generated, homogenous, turbulent flow field. An unheated and heated cylinder were considered with water, HFE-7100 ($C_4F_9OCH_3$, a fire protection hydrofluoroether by 3M[1] with a boiling point of 334 K), and HFE-7000 ($C_3F_7OCH_3$, with a boiling point of 307 K) serving as the working fluids. The common features of the two HFE agents are listed in Table 1. A homogeneous turbulent flow field was used to simulate the turbulence experienced by sprays for a representative fire suppression scenario in an aircraft engine nacelle at reported airflow conditions [2]. The choice of the above conditions was motivated by recent efforts to develop and validate the subgrid droplet impact model of the VULCAN computational fluid dynamics (CFD) fire physics code for spray-clutter interactive environments [3].

A large body of literature exists for problems related to grid-generated turbulence, droplet transport in vortices, and droplet/spray impingement on surfaces, including single isolated droplet impingement on flat surfaces (e.g., [4]) and cylinders (e.g., [5]), dripping liquid droplets off cylinders (e.g., [6, 7]), spray impingement on unheated and heated flat surfaces in different boiling regimes (e.g., [8–10]), droplet interactions with shear layers (e.g., [11]), and droplet entrainment in free turbulent flows (without impingement) to determine the influence of the flow on droplet trajectories (e.g., [12]). W. D. Bachalo and others [13, 14] have used phase Doppler interferometry to study droplet size–dependent interactions with the turbulent eddies formed on the leeward side of a cylinder. Estes and Mudawar [15] used phase Doppler interferometry to characterize a spray before impingement on a heated surface and to correlate the droplet mean size with the critical heat flux for spray surface cooling. The working fluids in their study included two Fluorinerts (i.e., FC-72 and FC-87), in addition to water.

Regarding the use of liquid fire suppressants in cluttered spaces, Takahashi et al. [16] and Grosshandler et al. [17] determined suppression efficiency in an obstructed passageway with a difficult to extinguish, bluff-body stabilized flame/pool fire configuration using gaseous, liquid, and solid powder fire suppressant alternatives. Examples of the characterization of liquid fire suppressants using phase Doppler interferometry include Yang et al. [18], who used various surrogate fluids to develop a liquid agent fire suppressant screen, studies of water-misted sprays and sprinkler systems (e.g., [19, 20]), and suppression of counterflow diffusion flames with water-based mists (e.g., [21, 22]). Recent work by Manzello and Yang [23, 24] studied impingement on a heated surface of water droplets containing sodium acetate trihydrate additive, which had similar physical properties to other known effective fire suppressant salts. They point out that studying the

_____

[1]Certain commercial equipment or materials are identified in this publication to specify adequately the experimental procedure. Such identification does not imply recommendation or endorsement by the National Institute of Standards and Technology, nor does it imply that the materials or equipment are necessarily the best available for this purpose.

Table 1   Selected Physical and Chemical Properties of the Agents Studied in This Investigation

Property	HFE7000[a]	HFE7100[a]	Water
Chemical formula	$C_3F_7OCH_3$	$C_4F_9OCH_3$	H_2O
Molecular weight (g mol^{-1})	200	250	18
Boiling point @ 1 atm (K)	307	334	373
Refractive index[b]	1.26	1.27	1.33
Liquid density @ 298 K (kg m^{-3})	1400	1481	995
Kinematic viscosity @ 298 K (mm^2 s^{-1})	0.32	0.37	1
Surface tension @ 298 K (kg s^{-2})	0.0124	0.0136	0.072
Specific heat @ 298 K (J kg^{-1} K^{-1})	1300	1183	4179
Themal conductivity @ 298 K (W m^{-1} K^{-1})	0.075	0.069	0.606
Global warming potential[c,d]	370	320	—
Ozone depletion potential[d]	0	0	—
Atmospheric lifetime (yr)	4.9	4.1	—

[a]   Supplied by the manufacturer.
[b]   At a temperature and pressure of 296 K, 101.3 kPa, and for wavelengths of 488.0 and 514.5 nm.
[c]   See Ref. [47] for definition.
[d]   See Ref. [48] for definition.

droplet impingement dynamics is important since one can conceive of a liquid fire suppressant impacting and cooling a surface as well as producing vapors that ultimately may entrain into and extinguish a fire. They also characterize the impact dynamics of HFE7100 because it was being screened, at the time, as a potential fire suppressant. Hung and Yao [6] and Hung [7] investigated numerically and experimentally the impact of droplet arrays and sprays on complicated arrangements such as screens, and the penetration of liquid through the gaps, for applications to fire suppression in compartments with complex openings. Recently, Disimile et al. [25] used phase Doppler interferometry to investigate the effects of clutter density of a spray impinging on a multilayer configuration of horizontal cylinders. In the present work, we complement this body of literature by focusing on droplet size–dependent effects during impingement and transport of a liquid spray onto and around a heated solid cylinder in a homogeneous turbulent gas flow, which was characterized using particle image velocimetry [26–28].

In previous experimental work, particle image velocimetry measurements were carried out to characterize gas-phase and water spray transport over cylinders of different diameters [27] and over a cylinder that was preheated to 423 K [26, 28] (i.e., above the boiling point of water, for the same turbulent flow conditions) to obtain the two-dimensional velocity field of the gas stream and water droplets. For the heated cylinder case, values of turbulence intensity were reported of up to about 8% for a total air supply flow rate of 440 kg/h [26, 28], which is typical of values expected in an engine nacelle [29]. The turbulent integral and Kolmogorov length scales are estimated to be approximately 12.7 mm (approximated by the characteristic dimension of the grid mesh size) and 150 μm, respectively [30–32], representing the range of length scales associated with this flow field. The obstacle used for the present study had a diameter larger than the integral length scale of turbulence. The results indicated that smaller droplets were entrained into the recirculation region downstream of the cylinder, while the larger droplets impacted the cylinder surface, accumulated and dripped off, rebounded off the surface, and dispersed outward into the free stream and/or were entrained in the free stream and transported around the surface. Vaporization of smaller droplets near the heated cylinder surface suggested an increased probability of vapor and a reduced probability of droplet entrainment into the cylinder wake region. These results indicated that droplet surface impact, vaporization, and transport behind the cylinder were dependent on droplet size. The present study expands this work to obtain quantitative information on droplet size using phase Doppler interferometry for different fire suppression fluids that embody a range of higher boiling points.

EXPERIMENTAL ARRANGEMENT

A photograph and schematic of the experimental apparatus is shown in Figs. 1 and 2 (Fig. 1 is a side view, and Fig. 2 is a front view). The experiment is oriented so that the flow issues horizontally to allow for the collection of liquid agent that drips off the cylinder and prevents liquid droplets downstream of the obstacle from falling back upstream into the oncoming flow. Droplets dripping off the cylinder were monitored by the rate at which they fell vertically downward into a large collection pan. The agents were supplied through a 60° solid-cone, pressure-jet atomizer (kept at room temperature), which generated a higher concentration of droplets in the center of the spray cone (Delavan type R-D nozzle). The orifice diameter is unknown since it is manufacturer proprietary information. The nominal water flow rate was 3.0 kg/h ± 0.35 kg/h at a line pressure immediately upstream of the atomizer of 791 kPa ± 65 kPa.[2] The pressure was held constant for the two HFE agents so that liquid atomization would be comparable (thus the flow rates varied according to the change in liquid density; see Table 1). Characterization of the atomizer was only carried out to the extent of providing initial conditions for the modeling effort; data are reported in Appendix A. A high-resolution digital camera provided still images and movies (at 9 frames/s) of the spray. A high-speed digital camera (at 1000 frames/s) [23, 24] was used to record the

---

[2]Estimation of the measurement uncertainty is determined from statistical analysis of a series of replicated measurements (referred to as a type A evaluation of uncertainty) and from other means other than statistical analysis (referred to as a type B evaluation of uncertainty) [33], calculated as $2u_c$ (representing a level of confidence of 95 %), where u_c is the combined standard uncertainty. The value for u_c was estimated statistically by $sn^{-1/2}$, where s is the standard deviation of the mean and n is the number of samples (type A uncertainty, where n = 11) and from the manufacturer uncertainty (type B uncertainty), if available.
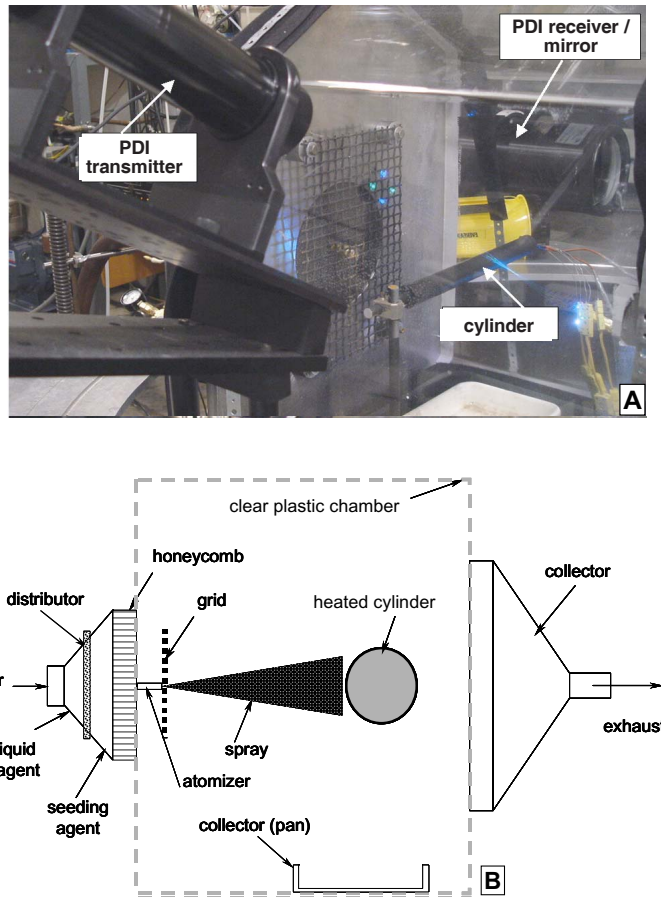
Fig. 1 Experimental arrangement for the droplet-laden, grid-generated turbulent flow field: (a) photograph and (b) schematic of the apparatus.

droplet impingement process on the cylinder. An octagon-shaped, clear plastic insert (with a wall thickness of 6 mm, a length of 610 mm, and major and minor axes of 760 mm and 560 mm for the cross section, respectively) was used as a boundary condition. The plastic insert, along with a front face that supported the inlet passages for the liquid agent and air and a back face that supported the exhaust passage, served to form a closed system at room temperature. For the present experiments, the incoming air (supplied at 301 kg/h ± 0.12 kg/h and providing a representative inlet air mean velocity of approximately 2.45 m/s) was directed entirely through a distributor plate with steel wool, a circular cross-sectional area of honeycomb to straighten the airflow, and then through a wire mesh screen, as illustrated in Fig. 1. The incoming air was adjusted to provide droplet mean velocities of about 4–5 m/s near the cylinder. The honeycomb had a 203-mm outer diameter (i.e., exposed to the downstream flow) and was 51 mm thick, with approximately 3-mm (length between opposite sides) hexagon-shaped cells. The honeycomb and wire mesh screen were copositioned around the atomizer (having a diameter of 17.8 mm), which resulted in removal of the central portion of the honeycomb (of an approximate area of 521.9 mm^2 ± 0.19 mm^2). The inlet air mean velocity was estimated by multiplying the honeycomb cell area by the approximated number of cells (3333 cells) exposed to the downstream flow field.

Grid-generated turbulence was imposed on the airstream by placing a square layer of wire mesh screen (with dimensions of 229 mm width by 330 mm length, 3.2 mm wire thickness, and 13 mm size cells) 25 mm downstream of the honeycomb. Note that the grid mesh covered the entire inlet area
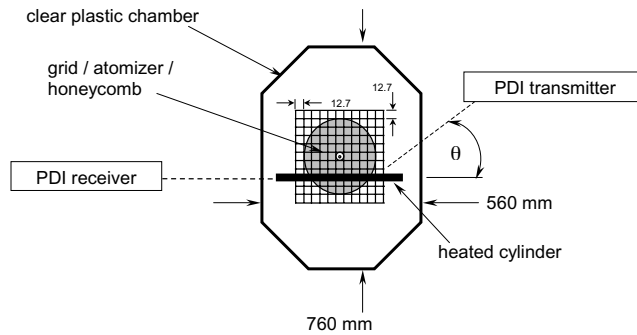
Fig. 2 Schematic of the experimental arrangement (upstream view) and orientation of the phase Doppler interferometer (PDI) with respect to the heated cylinder.

(compare the aforementioned honeycomb diameter to the grid dimensions). A schematic of the grid mesh pattern relative to the atomizer and incoming airflow is shown in Fig. 2. The rationale for the arrangement shown in Fig. 2 was discussed in detail elsewhere [27, 28]. Briefly, the grid mesh was placed downstream of any jetting of the airflow exiting the honeycomb. The face of the liquid atomizer was placed flush with the upstream side of the grid mesh and centered within one mesh cell so that the liquid spray would be unimpeded by the grid mesh. The grid Reynolds number was estimated to be 2019 for a streamwise air mean velocity of 2.45 m/s (for an air kinematic viscosity of 0.154 cm^2/s), as noted above, still in the turbulence regime for grid-generated turbulence [34]. A stepper motor–driven traversing system translated the entire experimental assembly, while the phase Doppler system was aligned at a stationary location (with the laser beams traversing the experimental arrangement parallel to the cylinder), independent of the traverse. This arrangement permitted measurements of the flow field properties at selected locations downstream of the injector and around the obstacle.

The cylinder, which formed the obstruction, was fabricated from a solid aluminum tube, with an outer diameter of 29.2 mm ± 0.04 mm and a length of 305 mm (see Fig. 3). Note that the cylinder had a length that did not span across the entire cross section of the chamber (to easily adjust its position relative to the spray nozzle), and a spanwise flow existed along the cylinder length. The spray impinged along the central portion of the cylinder and was estimated to cover up to approximately 183 mm of the cylinder upstream surface (taking into account the aforementioned spray angle, cylinder diameter, and atomizer/cylinder distance), well away from the edges. Entrainment of the droplets with the airflow will also reduce the dispersion of the spray. Thus, we confined our measurements to along the center plane to minimize any related edge effects. Surface heating was provided by a 13-mm-diameter hole bored through the center of the cylinder to accommodate a 250-W cartridge heater (13 mm in diameter and 76 mm in length). The
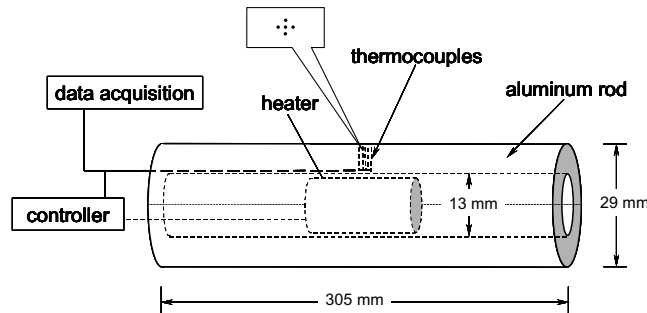
Fig. 3 Schematic of the cylinder with installed cartridge heater; the thermocouples on the upstream side of the cylinder were arranged in the cross pattern shown in the callout.

rod was split along its axis into two halves to allow 1-mm-deep channels to be milled along one segment for placement of five K-type thermocouples (Inconel sheathed, ungrounded, 0.8 mm in diameter and 305 mm in length). The thermocouple time response, as specified by the manufacturer, was 3 s at a level of confidence of 95%. The cylinder halves were bolted together and remachined to produce a seamless outer diameter. The thermocouples were placed in a cross pattern (see Fig. 3) in the center of the rod (each separated by a distance along the surface of 6.4 mm, with the thermocouple junctions placed about 3.2 mm of the surface from within bored holes at each location). The central thermocouple was used for temperature control of the heater, which was positioned behind the thermocouples. The expanded uncertainty for the temperature was 7.9 K, including the type B uncertainty of 3.1 K. The center of the cylinder was fixed at a location 187 mm ± 4 mm downstream of the grid mesh. Note that the farmost upstream position from the cylinder where data were obtained was 50.8 mm, which was about 136 mm downstream of the grid mesh. At this relatively large distance, heat transfer from the hot cylinder surface did not influence the initial experimental conditions.

PHASE DOPPLER INTERFEROMETER

Measurements were carried out using a two-component phase Doppler interferometer (PDI) with a Real-Time Signal Analyzer (RSA) available from TSI, Inc. [35, 36]. This PDI system is composed of the following components: (1) transmitter (model XMT204-4.3), (2) fiber drive (model FBD240-X), (3) receiver (model RCV216-X), (4) real-time signal processors (models RSA3200-P and RSA3200-L), (5) photomultiplier tube box (model RCM200P), and (6) RSA IO card version 3.0 (model RSA3CB2DV3). The PDI was controlled using TSI DataVIEW software version 2.02 run on a personal computer using the Windows NT operating system. The RSA has the ability to optimize the number of samples acquired-from the Doppler signal in real time. A 5-W argon ion laser operating in multiline mode was used as the illumination source. The blue (wavelength = 488 nm) and green (wavelength = 514.5 nm) lines of the argon ion laser were separated by beam conditioning optics and focused by the transmitting optics to intersect and form the probe volume. The transmitting optics are coupled to the beam conditioning optics using fiber optic cables to permit the transmitter to be located near the experiment. The front lens on the transmitter has a focal length of 500 mm. The green and blue beams have a beam separation distance of 39.9 mm and 40.2 mm, fringe spacing of 6.45 μm and 6.07 μm, and beam waist of 164 μm and 155 μm, respectively. Frequency shifting is set at 40 MHz. The receiver was located at a scattering angle, θ, of 30° measured from the direction of propagation of the laser beams (as specified by the manufacturer). To accommodate the horizontal orientation of the experimental apparatus, the transmitter and receiver were positioned in a vertical plane. Because of the large size of the receiver, the transmitter was positioned with the laser beams angled at 30° to the cylinder, which required correction of the cross-stream velocity by dividing its magnitude by the cosine of the angle. Also, a square mirror (305 mm × 381 mm) was used to direct the scattered laser light into the receiver. The front lens on the receiver had a focal length of 1000 mm. The spacing for the three photomultiplier tube detectors (A, B, and C) that are used to carry out the sizing measurements was 34.8 mm for detectors A and B and 101 mm for detectors A and C. A 150-μm slit aperture is located within the receiver to limit the length of the probe volume.

The setup procedure and normal systems tests for the optical arrangement were carried out as specified by the manufacturer [37], although the phase Doppler transmitter was set at 30° to the face of the chamber surface, and the scattered laser light by the droplets was collected by the receiver (which was normal to the chamber wall) via a mirror. For example, the transmitted beams were checked for changes in their polarization, that the beams lay coincident with each other inside the chamber, and that the collected light was properly focused on the receiver slit. A humidifier was placed inside the chamber to check the Doppler signal output and the measured size and velocity distributions. The droplet mean size and velocity were reproduced within 5% after comparing the measurements to prior results obtained with the humidifier without the chamber. The measurements were not checked at different positions along the chamber wall. The optical arrangement remained unchanged (including the scattering angle) for the different agents.

The signal processor was operated with the following settings: sample frequency of 40 MHz (the rate at which the Doppler signal is sampled), mixer frequency of 36 MHz (mixers are used to reduce the signal

frequency prior to analog-to-digital conversion), and low-pass filter setting of 20 MHz (low-pass filters are used to remove the summed components from the down-mixed signal so that only the difference is used). The settings were chosen to optimize the processor operation for the expected Doppler frequency, which is governed by the droplet velocity and fringe spacing. Hardware coincidence, which requires that droplets be detected on both PDI channels to be validated (with a maximum gate time of 200 µs), was used as an additional validation criterion for all measurements. Intensity validation (to remove particles whose scattered light intensities are too low and high and result in erroneous phase shifts and particle sizes) [38] and probe volume corrections (to account for droplets of varying size traveling through different sections of the Gaussian beam profile) were carried out to optimize the quality of the measurements.

Droplet size and velocity distributions were obtained at several cross-stream (R) positions and over a range of streamwise (Z) positions upstream and downstream of the cylinder. Measurements were not carried out along the spanwise direction of the cylinder (i.e., only along the cylinder center line in the R–Z plane, as defined in Fig. 4). Figure 4 illustrates the measurement grid and the location of the cylinder relative to the grid mesh. The measurement grid extended from approximately 50.8 mm upstream of the cylinder (approximately 136 mm downstream of the grid mesh) to a downstream position of 101.6 mm. An increment of 2.5 mm was used for –25.4 mm < Z < 38.1 mm, and an increment of 12.7 mm was used for all other streamwise positions. In the cross-stream direction, measurements were carried out in increments of 5 mm from 0 to 20 mm in the upper hemisphere (i.e., in the positive cross-stream direction). The total number of samples collected per measurement was set at 40,000, and the maximum acquisition time was 300 s. The time interval over which the actual data were collected varied with the density of the spray. For example, behind the cylinder, where droplets were absent, the total number of detected samples was not reached before the maximum acquisition time. However, for completeness, we include the measurements that did not reach the total number of samples. The refractive index was changed for each agent, as given in Table 1, and the measurements were carried out with the corresponding nondimensional slope value [25], i.e., 0.8275 (HFE7000), 0.8175 (HFE7100), and 0.761 (water).

Several strategies may be used to obtain size-dependent information of droplet transport around the cylinder. For example, a droplet with a negative streamwise velocity (i.e., a droplet transported against the flow) would be indicative of upstream transport. Such a result would be indicative of droplet entrainment in the recirculation zone for measurements carried out downstream of the cylinder or of droplet rebound for data obtained near the upstream surface of the cylinder. Size distributions devoid of relatively smaller droplets near the heated cylinder surface, as compared to locations away from the cylinder, may be indicative of the effects of vaporization. The following section presents data illustrating these aspects.

EXPERIMENTAL OBSERVATIONS

Images of the spray transport around the cylinder for the unheated and heated cases are shown in Fig. 5. These photographs were obtained using planar laser light illumination and the digital camera. The view
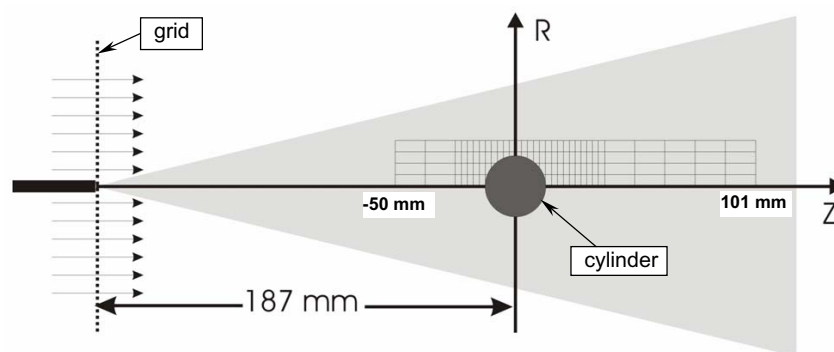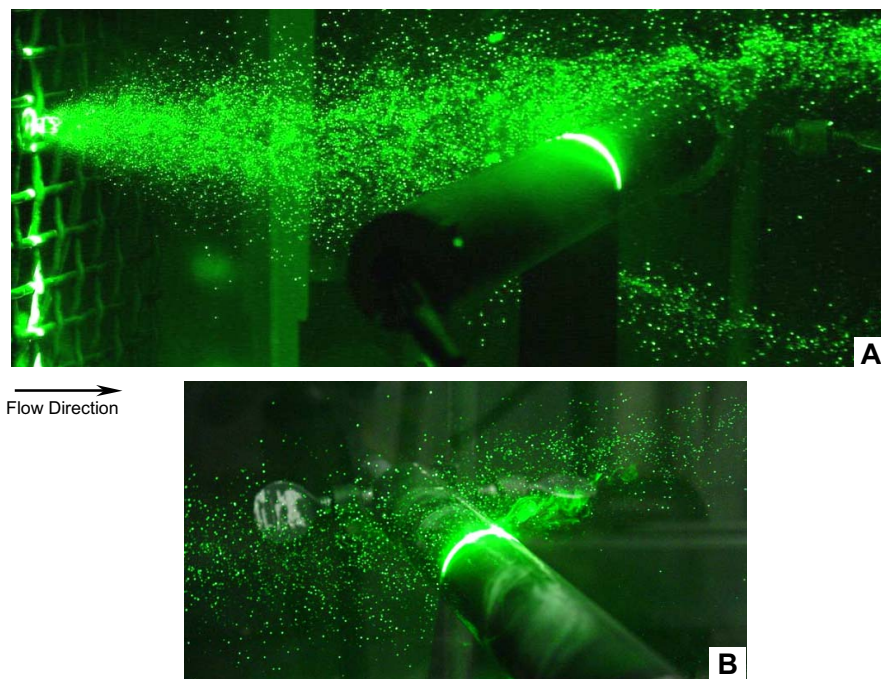

Fig. 4 Schematic of the measurement grid around the cylinder.

Flow Direction

Fig. 5   View of the (a) injected water spray over the unheated cylinder and the (b) injected water spray over the heated cylinder; the cylinder diameter is 29.2 mm.

in Fig. 5a is from the downstream side of the unheated cylinder, and that of Fig. 5b is from the upstream side of the heated cylinder. The bright "white" area around the cylinder is attributed to scattering of the laser light off the cylinder surface. For both cases, the cylinder appeared to act merely as an obstruction, blocking downstream transport of droplets. The heated cylinder shows evidence of droplet vaporization, as indicated by the vapor trail in the shear region downstream of the cylinder trailing edge (see Fig. 5b). Water droplets were observed in the center of the spray impinging on the cylinder surface and dripping off at the bottom, while droplets at larger cross-stream positions were transported around the cylinder. Many impinging droplets were observed in the high-speed movies to rebound off the surface and return to the free stream. Few larger-size water droplets (as defined by the relative light intensity noted in the images) were observed in the cylinder's wake, but this region was abundant with smaller-size droplets. There was no visual evidence of secondary breakup of the droplets (i.e., splashing). It was observed that water droplets dripped off the cylinder (not evident from Fig. 5) at a rate of approximately 6.5 mL/min for the unheated cylinder. Dripping of water droplets was not observed for the heated cylinder, presumably due to droplet vaporization. Droplets for the lower boiling point HFE suppressants were observed to vaporize readily, resulting in vaporization of droplets before reaching the unheated cylinder and the absence of dripping off the cylinder surface.

DROPLET SIZE AND VELOCITY MEASUREMENTS

The PDI was used to provide information on (1) droplets rebounding from the upstream face of the cylinder, (2) vaporization of droplets near the heated cylinder, (3) droplet sizes that are entrained into the recirculation region behind the cylinder, and (4) the effect of agent boiling point on droplet characteristics and transport. Figure 6 presents results of droplet Sauter mean diameter (D_{32}) and streamwise (U) and cross-stream (V) components of the mean velocity for water spraying onto the unheated cylinder. The rectangle located on the abscissa at a streamwise position of $Z \cong \pm 14.6$ mm represents the location of the
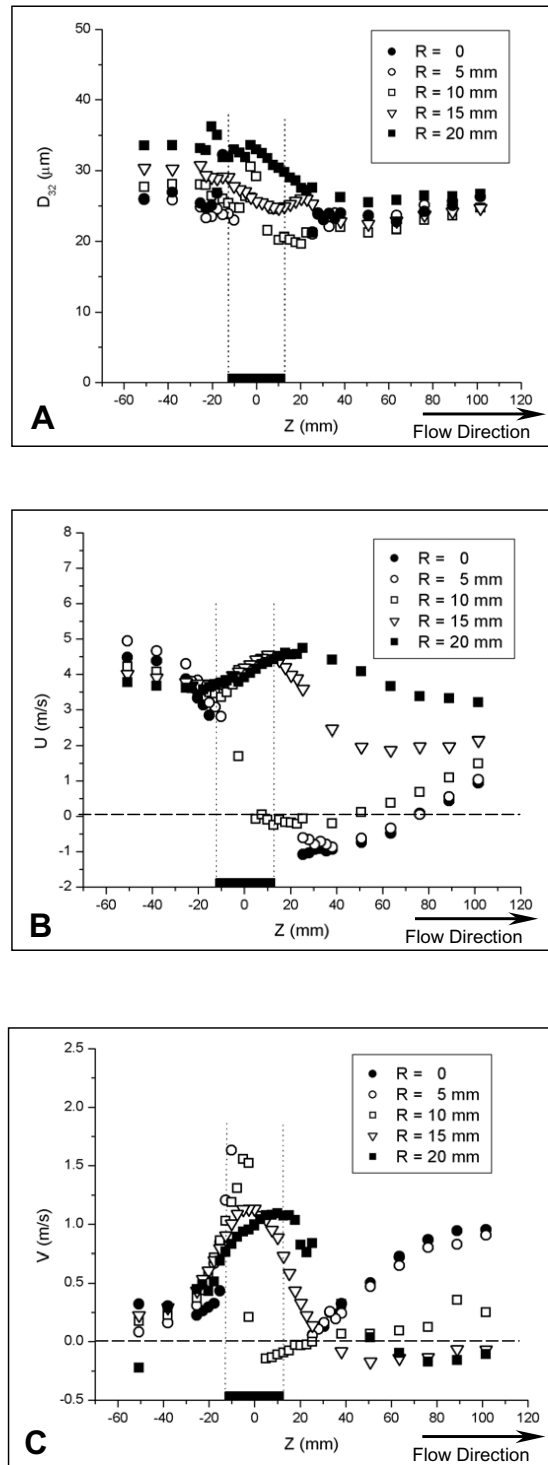
Fig. 6 Variation of water droplet (a) Sauter mean diameter (D_{32}), (b) mean streamwise velocity (U), and (c) mean cross-stream velocity (V) with streamwise position (Z) at different cross-stream positions (R) for the unheated cylinder.

cylinder, and the arrow indicates the direction of flow (see Fig. 4). Data for D_{32}, U, and V at $Z = -50$ mm (the upstreammost position of the measurement grid) and different cross-stream positions are given in Appendix A (see Tables A1 and A2) to provide initial conditions for model simulations. The type A evaluation of the standard uncertainty for D_{32} was 1.9 μm (7.4% of the mean value), and for U, it was 0.18 m/s (4.4% of the mean value). This uncertainty was estimated from the largest standard deviation of the mean (among standard deviations of the mean based on two replicates at each measurement location) throughout the measurement domain. The type B evaluation is more difficult to estimate and is discussed in detail by Widmann [20] and Widmann and Presser [39]. The gap in the data for the cross-stream positions $R = 0$, 5, and 10 mm indicates the presence of the cylinder. For Fig. 6a, the general trends are (1) a decrease in mean size on the downstream side of the cylinder, as compared to the upstream side, and (2) an increase in mean size with increasing cross-stream distance from the central plane of the cylinder on the upstream side (there is little change in the values of D_{32} with cross-stream distance far downstream of the cylinder). The latter trend is indicative of the presence of more smaller-size droplets near the center of the spray, in particular at $Z = -50$ mm, which is attributed to the design characteristics of the atomizer. One might argue that the increase in mean droplet size with radial position is due to the droplet gradation phenomenon [40] caused by the entrainment of the coaxial flow of air and not to the nozzle design. However, results obtained at $Z = -167$ mm (20 mm downstream of the atomizer; see Table A3) also show the same trend, and it is thus unlikely that this trend is due to air entrainment because of the relatively high momentum of the droplets at this location. Figure 6a indicates that there is a relatively small variation in droplet mean diameter with streamwise position upstream and downstream of the cylinder, but a distinct decrease in the values of D_{32} is present across the cylinder (see the black-squared curve for $R = 20$ mm). This effect is attributed to deflection of larger droplets by the cylinder outward from the central region of the spray (see Fig. 5a), which results in a bias toward smaller-size droplets being transported around the cylinder.

For the droplet streamwise mean velocity (see Fig. 6b), the values of U decrease with increasing cross-stream position, upstream at $Z = -50$ mm (also see the size and velocity distributions presented in Tables A1 and A2). The higher velocities near the center of the spray correlate with the smaller droplet mean size at this location, which again is argued [40] to be attributed to the larger droplets that shield the smaller droplets from the surrounding air, and thus the smaller droplets are susceptible to less drag and retain their original momentum. As the droplets approach the upstream surface of the cylinder, there is a decrease in the streamwise velocity component (see Fig. 6b) and an increase in the cross-stream component (see Fig. 6c), which is attributed to turning of the flow away from the cylinder stagnation plane. The streamwise and cross-stream mean velocity components increase with streamwise position (see the black-squared data for $R = 20$ mm in Figs. 6b and 6c) because of acceleration of the airflow around the cylinder [26, 27]. Likewise, the two components of velocity decrease downstream past the cylinder. The negative velocities (i.e., data below the dashed line in Fig. 6b) for $R = 0$, 5, and 10 mm are indicative of droplet entrainment into the recirculation zone downstream of the cylinder. Data were not obtained immediately downstream of the cylinder (i.e., for ≈14.6 mm < Z < 25 mm) at $R = 0$, 5, and 10 mm because the signals were too low to detect any droplets (presumably due to low concentration of droplets in this region). Farther downstream of the cylinder, at $Z = 101$ mm (see Fig. 6b), the streamwise velocities along the center line, although positive, are lower than for droplets at the larger cross-stream locations because of the influence of the recirculation zone on droplet transport. It appears that at distances beyond the measurement range, both the droplet mean sizes and velocities are asymptotically becoming independent of cross-stream position.

At locations near the upstream surface of the cylinder, negative values for the streamwise velocity for several individual droplets were detected (although the mean velocity is positive), which were indicative of upstream transport due to impingement and deflection (i.e., rebounding) of droplets off the surface. These results are evident in Fig. 7, which presents the correlation between the streamwise and cross-stream velocity components at $R = 0$ and $Z = -15$ mm. Note that the symbol diameters in the figure are droplet size–classified (i.e., the circle diameter is linearly related to the measured droplet diameter), and the legend provides a reference. Positive values of velocity are obtained for the abundance of droplets, which indicates that these impinging droplets either adhere to the cylinder surface or rebound at an angle that maintains their momentum in the downstream direction over the cylinder.

Flow field turbulence is thought to influence temporally droplet impingement on the cylinder surface and/or transport around the cylinder. Droplet drag, deceleration, and penetration through the flow field will
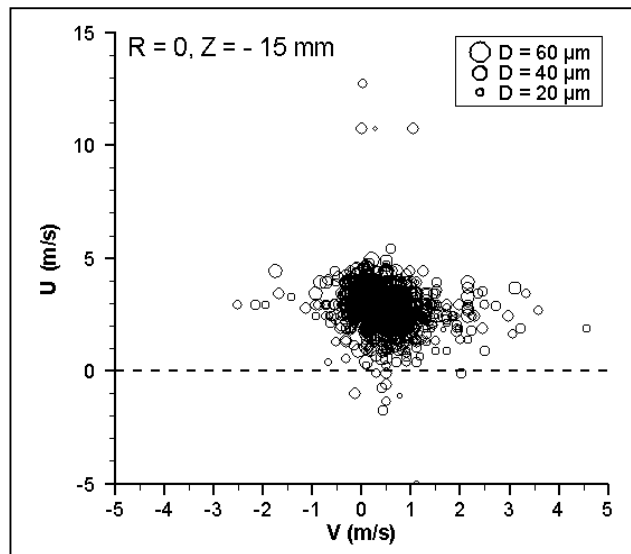
Fig. 7 Variation of the water streamwise velocity (U) with the cross-stream velocity (V) at the streamwise position of $Z = -15$ mm along the center line; the symbol diameters are droplet size–classified, and the dashed line highlights the presence of rebounded droplets (for $U < 0$).

vary with droplet Reynolds number [41]. The droplet Stokes number (St) provides a measure of whether droplet transport through the flow field will be unperturbed or responsive to the turbulent eddies [42]. Small-scale local turbulence may cause local diffusion (as characterized by the flow upstream of the cylinder), but large-scale turbulent structures are the primary dispersion mechanism (as characterized by the recirculation region downstream of the cylinder). The Stokes number is defined as St = $\rho D^2 u'/18\mu l$, where ρ is droplet density, D is droplet diameter, u' is the characteristic velocity (i.e., the root mean square of the turbulence fluctuations for small-scale turbulence or the relative velocity between the droplet and surrounding air for large-scale turbulence), μ is the air dynamic viscosity, and l is the characteristic turbulent eddy length scale. The interaction of turbulent eddies with individual droplets is dependent on droplet diameter and the turbulence length scales; in our case, the largest droplets (about 100 µm) are smaller than the reported Kolmogorov length scale, and the velocity fluctuations are generally smaller than the mean value [28]. This implies that a droplet will only experience temporal variations from the local free stream velocity, as discussed above, but will not experience nonuniformity in the local velocity field around the droplet (quasisteady droplet motion) [43]. Estimation of the Stokes number immediately upstream of the cylinder at $Z = -15.24$ mm and $R = 0$ and 20 mm indicated that when the Kolmogorov length scale is used (for an assumed root mean square velocity of 0.5 m/s [28]) then St < 1 (i.e., the droplets are influenced by the turbulent motion) only for droplet diameters smaller than about 10 µm. When the integral length scale is assumed, then St < 1 for all the detected droplets at these two locations. Estimation of the Stokes number downstream of the cylinder in the recirculation region at $Z = 25.4$ mm and $R = 0$ (for an assumed characteristic length scale of half the cylinder diameter and air velocity of -1.0 m/s [28]) found that St < 1 for all the detected droplets, indicating that the droplets are influenced by the large-scale turbulence.

As discussed earlier, the magnitude of the droplet streamwise mean velocity is negative for positions downstream of the cylinder, indicating the presence of a recirculation region. However, the mean velocity is representative of a distribution of individual droplet velocities and associated droplet sizes. This point is highlighted in Fig. 8, which presents the droplet streamwise velocity with respect to droplet interarrival time into the probe volume at two points downstream of the cylinder within the recirculation region. One measurement location at $R = 0$ and $Z = 25$ mm (see Fig. 8a) represents a measurement close to the downstream side of the cylinder (where the mean value is negative; see Fig. 6b), while the other, at $R = 0$

and $Z = 101$ mm (see Fig. 8b), represents a location near the downstream edge of the recirculation pattern (where the mean value is positive). The results for $Z = 25$ mm indicate that many droplets are recirculated upstream toward the cylinder (because $U < 0$), but they also indicate that several droplets at this location are transported in the downstream direction (i.e., $U > 0$). One can speculate that these latter droplets either originate in the recirculation zone or are transported around the cylinder surface and penetrate directly into the recirculation region. The cross-stream velocity component indicates that both positive and negative values are obtained for this group of droplets and may be indicative of droplets originating from either hemisphere of the cylinder (see Fig. 9a, which presents the correlation between the streamwise and cross-stream mean velocity components along the center line at $Z = 25$ mm). In addition, droplet diameter will not provide additional information on droplet transport since the size range for these positive axial velocity droplets varies between 5 μm and 35 μm, which is approximately the same range as for the entire population (i.e., for all the detected droplets at this position; see Fig. 9b, which presents the correlation between the streamwise mean velocity component and droplet diameter along the center line at $Z = 25$ mm). In a similar vein, the results for $Z = 101$ mm (see Fig. 8b) indicate that the abundance of droplets are transported in the downstream direction at this point (i.e., for $U > 0$), however, several droplets are still entrained into the recirculation region (i.e., for $U < 0$). Again, the cross-stream velocity component indicates that both positive and negative values are present at $Z = 101$ mm (see Fig. 9c, which presents the streamwise/cross-stream velocity correlation along the center line at $Z = 101$ mm) and that the size range of recirculated droplets is between 5 μm and 35 μm (see Fig. 9d, which presents the correlation between the streamwise mean velocity component and droplet diameter along the center line at $Z = 101$ mm). These results are indicative of droplet transport at the downstream edge of the recirculation zone.

Comparison of the Unheated and Heated Cylinders

Comparison of results for the unheated and heated cylinders for the complete set of profiles is shown in Fig. 6. As an example, the unheated and heated results are compared in Fig. 10 for $R = 0$ and 20 mm. The results indicate consistently that the droplet Sauter mean diameter, D_{32}, is smaller for the heated cylinder (for droplets both upstream and downstream of the cylinder; see Figs. 10a and 10c). The droplet streamwise velocity component is also lower for the heated cylinder (see the data upstream of the cylinder in Fig. 10b and the entire profile for Fig. 10d). These changes are attributed to the heat transfer from the cylinder, which reduces droplet diameters through vaporization and correspondingly diminishes the droplet velocity since smaller droplets decelerate quicker than the larger ones. One must also consider
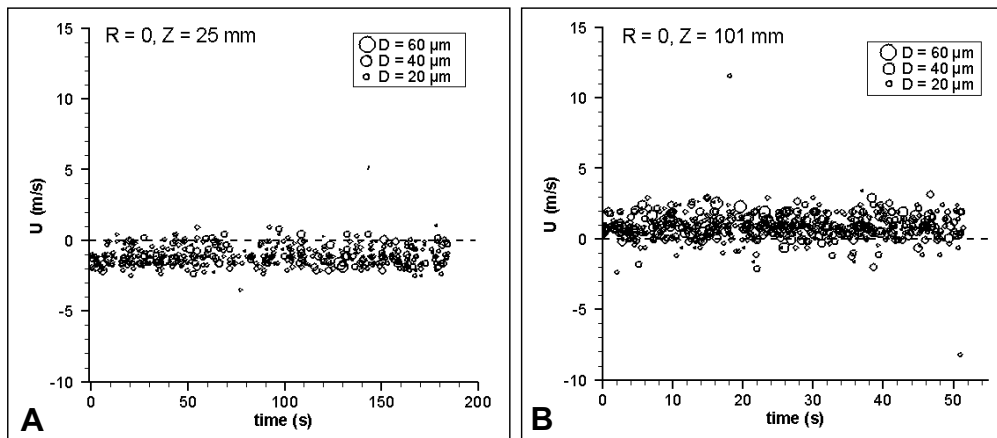
Fig. 8 Variation of the water streamwise velocity (U) with interarrival time at two streamwise positions of (a) $Z = 25$ mm and (b) $Z = 101$ mm along the center line, downstream of the unheated cylinder within the recirculation region; the symbol diameters are droplet size–classified, and the dashed line highlights the presence of recirculated droplets (for $U < 0$).
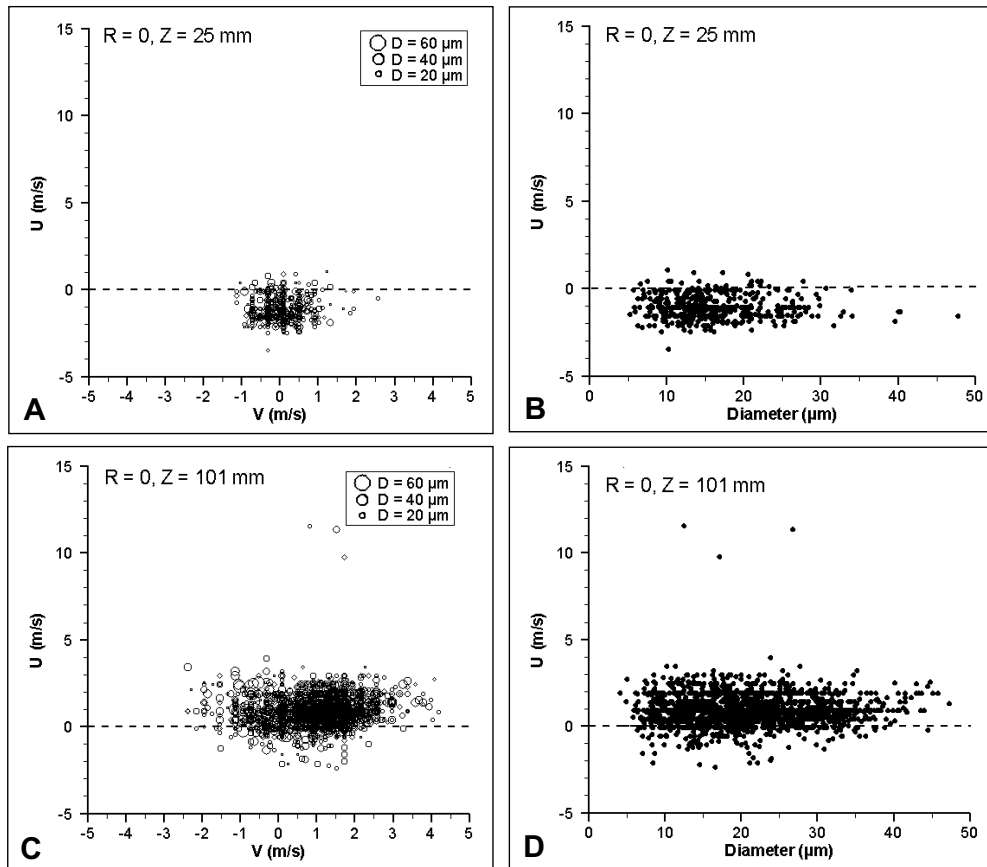
Fig. 9 Correlation between the water streamwise (U) and cross-stream (V) mean velocity components along the center line at (a) $Z = 25$ mm and (b) $Z = 101$ mm and the correlation between the streamwise mean velocity and droplet diameter (D) at (c) $Z = 25$ mm and (d) $Z = 101$ mm; the symbols in Figs. 9a and 9b are droplet size–classified; Figs. 9c and 9d have a fixed symbol size; and the dashed line highlights the presence of recirculated droplets (for $U < 0$).

the effect of the gas temperature on other parameters of the drag force, such as the physical properties of air, which will affect droplet decerleration. Downstream of the cylinder for $R = 0$, droplets are entrained in the recirculation zone (see the data below the dashed line in Fig. 10b), and the magnitude of the negative streamwise velocity component in this region is smaller for the heated case, which is consistent with a weaker recirculation zone. The decrease in both D_{32} and U for the heated case indicates that droplet vaporization does not result in the complete removal of the smaller-size droplets from the distribution (which could result in an increase in the mean size and velocity) but instead in a decrease in the size of all droplets (which results in an overall decrease in both the mean size and velocity). In fact, the droplet size distributions illustrate clearly the shift of the entire distribution (without any significant change in the distribution skewness) to smaller sizes for the heated cylinder. An example of this change in the size distributions is given in Fig. 11 at $R = 20$ mm and $Z = 0$.

As stated earlier, there was no visual evidence of secondary breakup of droplets (i.e., splashing), which was expected because the Weber number (i.e., We = 28 for a 100-μm water droplet with a streamwise velocity of 4.5 m/s; see Table A1 for the unheated cylinder) was estimated to be much smaller than the critical value for droplet shattering [3, 44]. For water droplet impingement (Leidenfrost temperature of 603 K) on a heated, stainless steel, flat surface (for Weber numbers of 74 and 171), Manzello and Yang [23] observed that a droplet in the film boiling regime (i.e., above the Leidenfrost
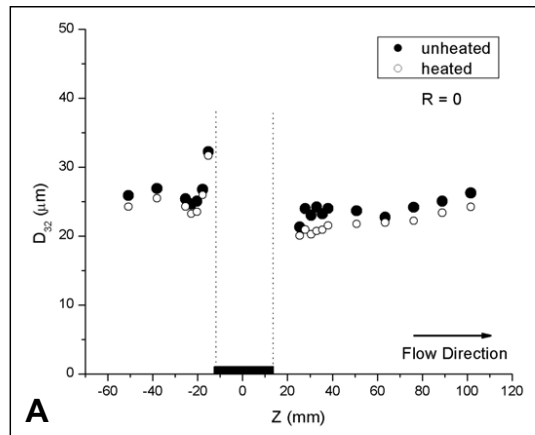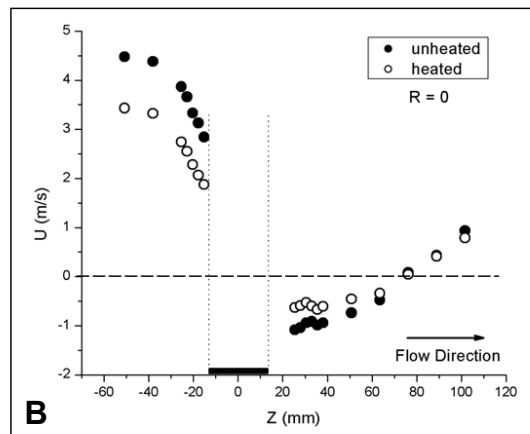
Fig. 10a

Fig. 10b
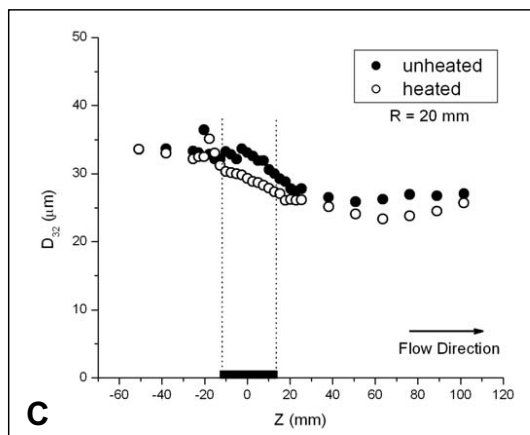

Fig. 10c

Fig. 10   Variation of the water droplet Sauter mean diameter at (a) $R = 0$ and (c) $R = 20$ mm and the mean streamwise velocity at (b) $R = 0$ and (d) $R = 20$ mm, with streamwise position (Z) for the unheated and heated cylinders.
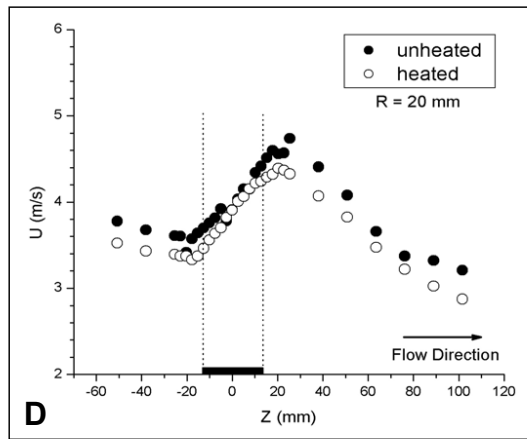
Fig. 10d

temperature) will readily break up into a cellular structure, forming many smaller satellite droplets that rebound off the surface. Droplet sizes used for their experiments were on the order of millimeters, while, as stated earlier, rebounding droplets for the experiments reported here were generally smaller than 35 μm. Manzello and Yang [23] showed that for droplet impingement on an unheated surface, droplets were found to wet the surface. Since the heated cylinder in the present investigation was at 423 K, secondary breakup and droplet rebounding would be unlikely to occur for water droplets impinging the cylinder. Recent studies advocate the use of a droplet impact number, K (= $We^{0.5}Re^{0.25}$), which is compared to a
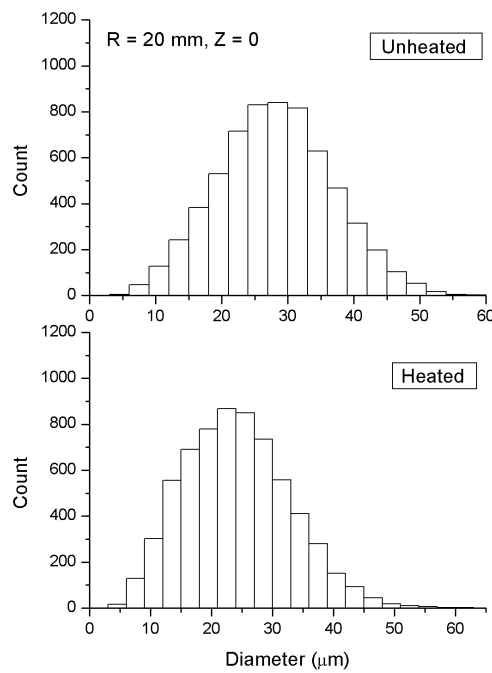

Fig. 11 Comparison of the water droplet size distribution for both the unheated and heated cylinder at R = 20 mm and Z = 0.

critical value, K_{crit} [45, 46], for which shattering will occur, $K > K_{crit}$. The value of K_{crit} is approximately 57.7 for rougher surfaces and increases to $K_{crit} \cong 132$ for smoother surfaces. For the work presented here, the cylinder surface was coated with flat black paint to reduce reflection from the laser beams of the phase Doppler instrument, and so the cylinder surface smoothness was not considered high. If we estimate K from mean values of droplet size and velocity, we find that for a 100-μm water droplet with a streamwise velocity of 4.5 m/s, $We \cong 28$, $Re_{droplet} \cong 448$, and therefore $K \cong 24$. However, if the value of K is determined for the individual detected droplets from the size and velocity distributions at the center line location obtained closest to the upstream side of the unheated cylinder (i.e., $R = 0$ and $Z = -15.2$ mm), then we find that for three droplets, $K > 57.7$, and for no droplets, $K > 132$. The largest value of K was approximately 103 ($We = 356$ and $Re = 893$) for a droplet diameter of about 31 μm and a corresponding streamwise velocity of 29 m/s. For the heated cylinder at the same aforementioned location, two droplets had values of $K > 57.7$ (no droplets for $K > 132$). The largest value of K was approximately 67 ($We = 175$ and $Re = 660$) for a droplet diameter of about 31 μm and a corresponding streamwise velocity of 29 m/s. Thus droplet shattering (and its influence on droplet size distribution) is considered improbable, even though a relatively few number of individual droplets in the spray may satisfy the criterion for secondary breakup and rebounding.

Comparison of Suppressants

Spray characteristics for the lower boiling point suppressants (i.e., the HFE agents) were compared with water using a new 60° solid-cone, pressure-jet atomizer (also a Delavan type R-D nozzle). Data for D_{32}, U, and V at $Z = -50$ mm and different cross-stream positions are given in Appendix A (see Table A2) to provide initial conditions for modelers. The Sauter mean diameter, streamwise, and cross-stream velocity components at 20 mm downstream of the atomizer (i.e., $Z = -167$ mm) are given in Table A3. The HFE agents (unlike for water) were observed to form a fine mist, resulting in few droplets impinging on the obstacle surface and the absence of liquid dripping from the unheated cylinder. As a result of the significantly reduced concentration of droplets reaching the cylinder, the heated cylinder case was not investigated since droplet transport and impingement would be further suppressed in the vicinity of the cylinder and below the detection threshold of the phase Doppler instrument.

Figure 12 presents a comparison of the droplet mean size, streamwise velocity, and cross-stream velocity with streamwise position for the three agents at $R = 0$ and 20 mm. Note that data were not
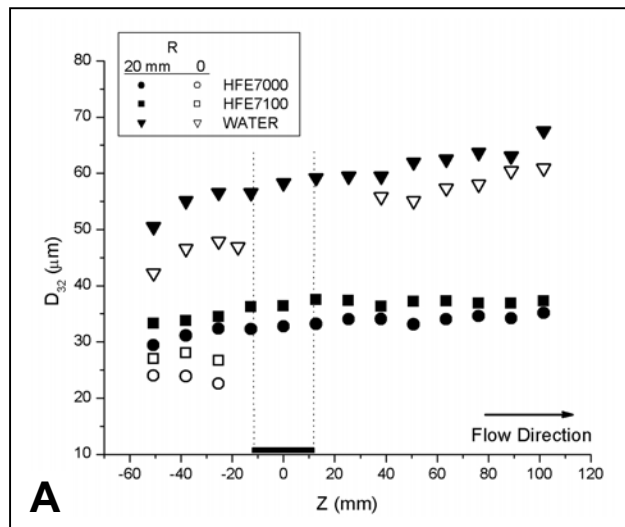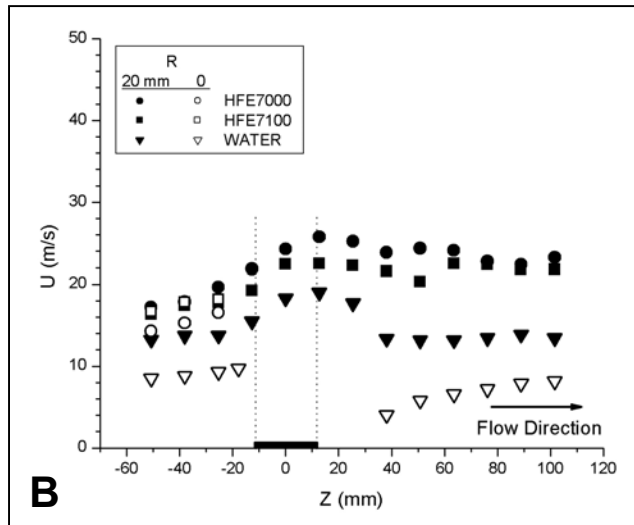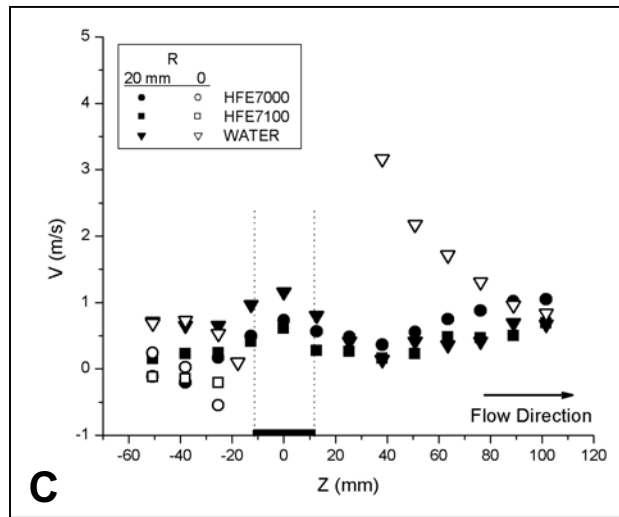

Fig. 12a

Fig. 12b

Fig. 12c

Fig. 12 Variation of the agent droplet (a) Sauter mean diameter, (b) mean streamwise velocity, and (c) mean cross-stream velocity with streamwise position (Z) at cross-stream positions of $R = 0$ and 20 mm for the three agents.

obtained downstream of the cylinder at $R = 0$ for the HFE agents, as discussed above. Also note that the values for D_{32} and U are generally larger than for the earlier water results reported above, which is attributed the new atomizer characteristics, even though all operating conditions were unchanged. At one point, the airflow rate was also increased to 663 kg/h (from the normal operating condition of 301 kg/h) in order to promote the shattering of droplets on surface impingement. However, there was no visual evidence to support shattering. Manzello and Yang [23, 24] also studied droplet impingement and rebounding for HFE7100 (Leidenfrost temperature of 413 K). Again, for the unheated cylinder, secondary breakup was unlikely to occur for water or HFE7100 at their maximum Weber numbers of 171 (for

water) and 750 (for HFE7100). However, determination of the value of K for individual droplets with size and velocity distributions at the center line location obtained closest to the upstream side of the cylinder (for the normal operating conditions) indicated the presence of few droplets with $K > K_{crit}$. There were 26 droplets with $K > 57.7$ and one droplet with $K > 132$ for water at $Z = -17.8$ mm, 17 droplets with $K > 57.7$ (no droplets for $K > 132$) for HFE7100 at $Z = -20.3$ mm, and 3 droplets with $K > 57.7$ (no droplets for $K > 132$) for HFE7000 at $Z = -25.4$ mm. The largest value of K for water was approximately 159 (We = 697 and Re = 1305) for a droplet diameter, D, of about 34 μm and a corresponding streamwise velocity, U, of 38 m/s; for HFE7100, $K \cong 112$ (We = 395, Re = 1004), $D \cong 36$ μm, and $U \cong 28$ m/s; and for HFE7000, $K \cong 73$ (We = 208, Re = 660), $D \cong 29$ μm, and $U \cong 23$ m/s. Again, it is unlikely that individual droplet shattering and rebounding will influence significantly droplet size distributions for the three agents and operating conditions used in this study.

The results at the normal operating conditions (with the airflow rate of 301 kg/h) indicated a clear trend for the effect of suppressant boiling point on droplet size and velocity. Comparison of results for the three agents in Fig. 12 indicates that droplet mean size increases and streamwise velocity decreases with an increase of agent boiling point. Although the agent boiling point influences droplet vaporization (with the HFE agents vaporizing more readily than water), it should not be implied that agent boiling point exerts the only effect on droplet size and velocity. One could also explain the variation in droplet mean diameter shown in Fig. 12 by the fact that the water viscosity and surface tension are larger than for the HFE agents (see Table 1) and that the water droplet velocities are expected to be smaller than the HFE agents due to the higher viscosity and lower density of water relative to the HFE agents. Note one exception for the HFE7100 streamwise velocity profile in Fig. 12b at $R = 0$ (open squares on the upstream side of the cylinder), where the values are higher than those for HFE7000 (open circles); it is unknown why the HFE7100 velocities were higher than expected. The size distribution for each agent was also found to shift to larger sizes for increasing agent boiling point (see Fig. 12a), which is indicative of reduced droplet vaporization with increasing agent boiling point. An example of this shift in droplet size distribution is given in Fig. 13, which compares the three agents at $R = 20$ mm and $Z = 0$. Note that the
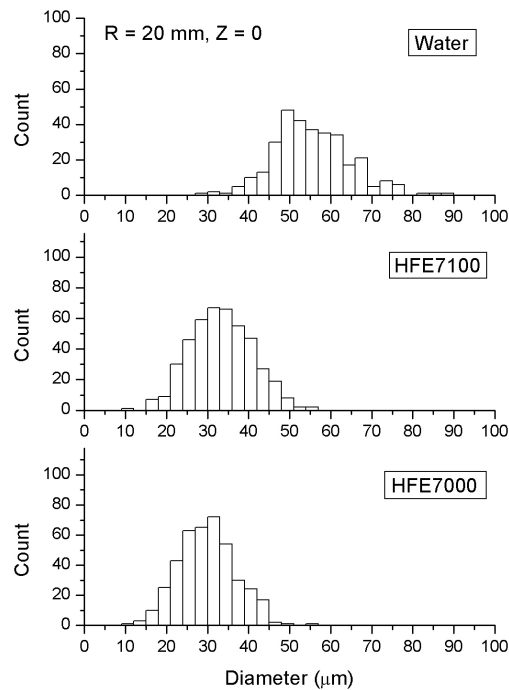
**Fig. 13** Comparison of the agent droplet size distribution for the three agents at $R = 20$ mm and $Z = 0$.
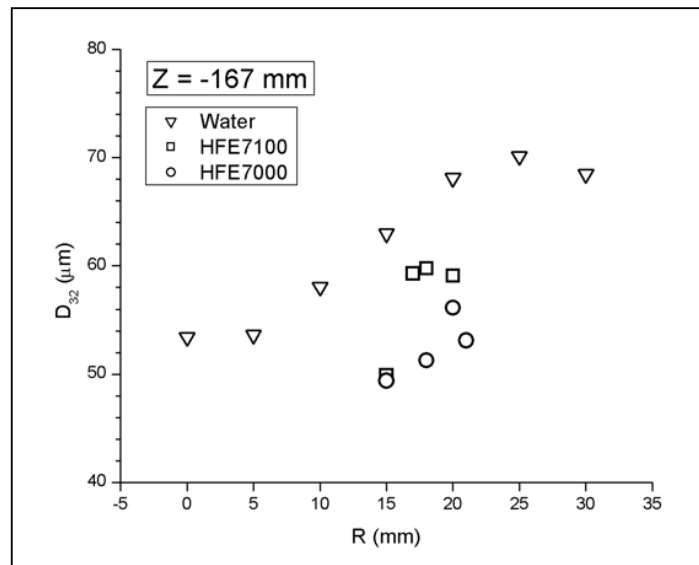
Fig. 14 Variation of Sauter mean diameter (D_{32}) with radial position (R) at $Z = -167$ mm (i.e., 20 mm downstream of the atomizer) for the three agents (replacement atomizer) (See Table A3).

results near the atomizer exit at $Z = -167$ mm (see Table A3) indicate that the Sauter mean diameter increases with increasing agent boiling point (see Fig. 14), but there was a negligible change in the velocity components. It is understandable that the droplet mean diameter is larger for water than for the HFE agents, as reported above. However, one would also expect the water droplet velocities to be smaller than the HFE agents for the same upstream supply pressure.

Comparing results for the two cross-stream positions presented in Fig. 12 indicates that D_{32} and U increase for increasing values of R, which is expected (i.e., larger droplets are correlated with higher velocities) and which is similar to the results obtained for the original atomizer (see Fig. 6). Downstream of the cylinder, the Sauter mean diameter continues to increase, unlike the results reported for the original atomizer (compare the change in D_{32} over the cylinder with Fig. 6a), while the streamwise mean velocity does change in a similar fashion. This increase in Sauter mean diameter is attributed to the higher droplet streamwise velocities associated with this atomizer. The presence of larger droplets and higher droplet velocities downstream of the cylinder result in more ballistic trajectories in the streamwise direction and fewer droplets entrained in the recirculation zone (which remained unchanged for the given airflow rate). As a result, larger droplets are present at the measurement locations downstream of the cylinder for this new atomizer (even with droplet rebounding off the cylinder surface). This point is substantiated by results at $R = 0$ and $Z = 38$ mm for water (see Figs. 12a and 12b), which is the closest location downstream of the cylinder along the center line, where detectable phase Doppler signals provided a valid measurement (for the original nozzle, this location corresponded to $R = 0$ and $Z = 25$ mm; see Fig. 6). Figure 15 presents the streamwise/cross-stream velocity correlation at this position and indicates that only a few droplets are detected with negative streamwise velocities (i.e., recirculated droplets), whereas an abundance of recirculated smaller droplets were present downstream of the cylinder for the original atomizer (see Fig. 9a).

CONCLUSIONS

Phase Doppler measurements were carried out to obtain droplet size and velocity distributions in a droplet-laden homogenous turbulent flow field around a cylindrical obstacle. Results indicated that most
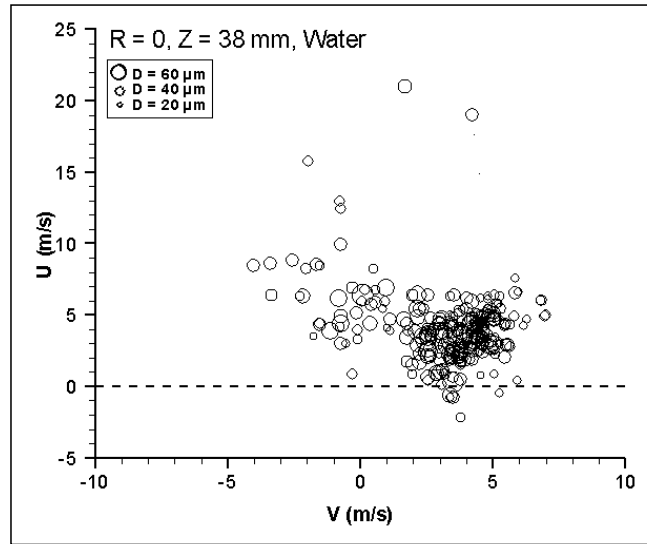
Fig. 15 Correlation between the streamwise (U) and cross-stream (V) velocity components along the center line at $Z = 38$ mm for water; the symbol diameters are droplet size–classified, and the dashed line highlights the presence of recirculated droplets (for $U < 0$).

impinging droplets adhere to the surface, with few droplets rebounding back into the free stream. Rebounding droplets are generally less than 35 μm, corresponding to the higher probability portion of the size distribution. Downstream, in the wake region of the cylinder, a distribution of smaller-size droplets (generally, of less than 35 μm) is entrained in the recirculation zone. Droplets larger than 35 μm tend to impinge on the cylinder surface or disperse around the cylinder to be transported far downstream of the obstacle. Near the heated cylinder surface, water droplet vaporization results in smaller droplet mean sizes and lower velocities, as compared to the ambient case. Droplets from lower boiling point suppressants tend to vaporize more readily, resulting in vaporization of droplets before reaching the obstacle and in the absence of dripping off the cylinder surface. Droplet size increases and velocity decreases with increasing agent boiling point, however, these variations may also be explained by the changes in agent physical properties. It is improbable that shattering occurs for the droplet sizes and velocities encountered with the given operating conditions, however, it is conceivable that shattering may occur for a few individual impinging droplets.

REFERENCES

1. P. Andersson and G. Holmstedt, Limitations of Water Mist as a Total Flooding Agent, *J. Fire Protec. Eng.*, vol. 9, pp. 31–50, 1999.
2. J. Dolinar, D. Hudgins, and D. Keyser, F-18 E/F Nacelle Simulator Input/Output Boundary Condition Flows, Naval Air Warfare Cent. Rep. A176214 (INS/F-18-1), Lexington Park, MD, 2002.
3. S. S. Yoon, P. E. DesJardin, C. Presser, J. C. Hewson, and C. T. Avedisian, Numerical Modeling and Experimental Measurements of Water Spray Impact and Transport Over a Cylinder, *Int. J. Multiphase Flow,* vol. 32, pp. 132–157, 2006.
4. S. Chandra and C. T. Avedisian, On the Collision of a Droplet with a Solid Surface, *Proc. R. Soc. London, Ser. A*, vol. 432, pp. 13–41, 1991.
5. M. Pasandideh-Fard, M. Bussmann, S. Chandra, and J. Mostaghimi, Simulating Droplet Impact on a Substrate of Arbitrary Shape, *Atomization and Sprays*, vol. 11, pp. 397–414, 2001.
6. L. S. Hung and S. C. Yao, Experimental Investigation of the Impaction of Water Droplets on Cylindrical Objects, *Int. J. Multiphase Flow*, vol. 25, pp. 1545–1559, 1999.

7. L. S. Hung, Investigations of the Transport and Dynamics of Droplets Impacting on Complex Objects, Ph.D. dissertation, Department of Mechanical Engineering, Carnegie Mellon University, Pittsburgh, PA, 1998.

8. J. E. Gonzales and W. Z. Black, Study of Droplet Sprays Prior to Impact on a Heated Horizontal Surface, *J. Heat Transfer*, vol. 119, pp. 279–287, 1997.

9. S. C. Yao, Dynamics and Heat Transfer on Impacting Sprays, in C. L. Tien (ed.), *Annual Review of Heat Transfer*, vol. 5, chap. 8, CRC Press, Boca Raton, FL, 1994.

10. C. Tropea and I. V. Roisman, Modeling of Spray Impact on Solid Surfaces, *Atomization and Sprays*, vol. 10, pp. 387–408, 2000.

11. C. T. Crowe, J. N. Chung, and T. R. Troutt, Particle Mixing in Free Shear Flows, *Prog. Energy Combust. Sci.*, vol. 14, pp. 171–194, 1988.

12. B. J. Lazaro and J. C. Lasheras, Particle Entrainment and Turbulent Mixing in Free, Shear-Flows: Part 1. The Naturally Developing Mixing Layer, *J. Fluid Mech.*, vol. 235, pp. 143–178, 1992.

13. W. D. Bachalo, R. C. Rudoff, and M. J. Houser, Laser Velocimetry in Turbulent Flow Fields: Particle Response, *Proc. 25th AIAA Aerospace Sciences Meeting & Exhibit*, Paper AIAA-87-0118, 1987.

14. G. Wang, E. J. Bachalo, S. V. Sankar, and W. D. Bachalo, An Investigation of Spray Interaction with Large-Scale Eddies, *Proc. 5th Annual Conf. on Liquid Atomization and Spray Systems*, pp. 53–58, 1992.

15. K. A. Estes and I. Mudawar, Correlation of Sauter Mean Diameter and Critical Heat Flux for Spray Cooling of Small Surfaces, *Int. J. Heat Mass Transfer*, vol. 38, pp. 2985–2996, 1995.

16. F. Takahashi, W. J. Schmoll, and V. M. Belovich, Suppression of Bluff-Body Stabilized Pool Flames, *Proc. 37th AIAA Aerospace Sciences Meeting & Exhibit*, Paper AIAA-99-0327, 1999.

17. W. Grosshandler, A. Hamins, K. McGrattan, S. R. Charagundla, and C. Presser, Suppression of a Non-premixed Flame Behind a Step, *Proc. Combust. Inst.*, vol. 28, pp. 2957–2964, 2000.

18. J. C. Yang, M. K. Donnelly, N. C. Privé, and W. L. Grosshandler, An Apparatus for Screening Fire Suppression Efficiency of Dispersed Liquid Agents, *Fire Safety J.*, vol. 36, pp. 55–72, 2001.

19. E. J. P. Zegers, B. A. Williams, R. S. Sheinson, and J. W. Fleming, Water Mist Suppression of Methane/Air and Propane/Air Counterflow Flames, *Proc. 10th Halon Options Technical Working Conf.*, pp. 251–261, 2000.

20. J. F. Widmann, Characterization of a Residential Fire Sprinkler Using Phase Doppler Interferometry, *Atomization and Sprays*, vol. 12, pp. 69–90, 2002.

21. A. M. Lazzarini, R. H. Krauss, H. K. Chelliah, and G. T. Linteris, Extinction Conditions of Non-premixed Flames with Fine Droplets of Water and Water/NaOH Solutions, *Proc. Combust. Inst.*, vol. 28, pp. 2939–2945, 2000.

22. E. J. P. Zegers, B. A. Williams, R. S. Sheinson, and J. W. Fleming, Dynamics and Suppression Effectiveness of Monodisperse Water Droplets in Non-premixed Counterflow Flames, *Proc. Combust. Inst.*, vol. 28, pp. 2931–2937, 2000.

23. S. L. Manzello and J. C. Yang, On the Collision Dynamics of a Water Droplet Containing an Additive on a Heated Solid Surface, *Proc. R. Soc. London, Ser. A*, vol. 458, pp. 2417–2444, 2002.

24. S. L. Manzello and J. C. Yang, An Experimental Study of High Weber Number Impact of Methoxy-Nonafluorobutane $C_4F_9OCH_3$ (HFE7100) and n-Heptane Droplets on a Heated Solid Surface, *Int. J. Heat Mass Transfer*, vol. 45, pp. 3961–3971, 2002.

25. P. J. Disimile, J. R. Tucker, B. Croswell, and J. Davis, The Transport of Water Sprays Past Generic Clutter Elements Found within Engine Nacelles, *Fire Safety J.*, vol. 40, pp. 65–78, 2005.

26. C. Presser, G. Papadopoulos, and J. F. Widmann, Droplet-Laden Homogeneous Turbulent Flow Past Unheated and Heated Cylinders, *Proc. ASME/JSME Joint Fluids Engineering Conf. (FEDSM'03)* [CD-ROM], Paper FEDSM2003-45240, 2003.

27. C. Presser, J. F. Widmann, P. E. DesJardin, and L. A. Gritzo, Measurement and Numerical Prediction of Homogeneous Turbulent Flow over a Cylinder: A Baseline for Droplet-Laden Flow Studies, *Proc. 40th AIAA Aerospace Sciences Meeting & Exhibit*, Paper AIAA 2002-0905, 2002.

28. C. Presser, J. F. Widmann, and G. Papadopoulos, PIV Measurements of Droplet Transport in a Homogeneous Turbulent Flow over a Cylinder, *Proc. 41st AIAA Aerospace Sciences Meeting and Exhibit*, Paper AIAA 2003-0846, 2003.

29. P. E. DesJardin, J. M. Nelsen, L. A. Gritzo, A. R. Lopez, J. M. Suo-Anttila, D. R. Keyser, T. A. Ghee, P. J. Disimile, and J. R. Tucker, Towards Subgrid Scale Modeling of Suppressant Flow in Engine Nacelle Clutter, *Proc. 11th Halon Options Technical Working Conf.*, pp. 99–110, 2001.

30. S. B. Pope, *Turbulent Flows*, Chapter 6, Cambridge University Press, New York, 2000.

31. W. H. Snyder and J. L. Lumley, Some Measurements of Particle Velocity Autocorrelation Functions in a Turbulent Flow, *J. Fluid Mech.*, vol. 48, pp. 41–71, 1971.

32. M. R. Wells and D. E. Stock, The Effects of Crossing Trajectories on the Dispersion of Particles in a Turbulent Flow, *J. Fluid Mech.*, vol. 136, pp. 31–62, 1983.

33. B. N. Taylor and C. E. Kuyatt, Guidelines for Evaluating and Expressing the Uncertainty of NIST Measurement Results, NIST Tech. Note 1297, Gaithersburg, MD, 1994.

34. M. van Dyke, *An Album of Fluid Motion*, Parabolic Press, Stanford, CA, pp. 88–89, 1982.

35. W. D. Bachalo and M. J. Houser, Development of the Phase/Doppler Spray Analyzer for Liquid Drop Size and Velocity Characterizations, *Proc. AIAA/SAE/ASME 20th Joint Propulsion Conf.*, Paper AIAA-84-1199, 1984.

36. W. D. Bachalo and M. J. Houser, Phase/Doppler Spray Analyzer for Simultaneous Measurements of Droplet Size and Velocity Distributions, *Opt. Eng.*, vol. 23, pp. 583–590, 1984.

37. TSI/Aerometrics, *Phase Doppler Particle Analyzer Operations Manual*, Sunnyvale, CA, 1999.

38. J. F. Widmann, C. Presser, and S. D. Leigh, Extending the Dynamic Range of Phase Doppler Interferometry Measurements, *Atomization and Sprays*, vol. 12, pp. 513–537, 2002.

39. J. F. Widmann and C. Presser, A Benchmark Experimental Database for Multiphase Combustion Model Input and Validation, *Combust. Flame*, vol. 129, pp. 47–86, 2002.

40. S. S. Yoon, J. C. Hewson, P. E. DesJardin, D. J. Glaze, A. R. Black, and R. R. Skaggs, Numerical Modeling and Experimental Measurements of a High Speed Solid-Cone Water Spray for Use in Fire Suppression Applications, *Int. J. Multiphase Flow*, vol. 30, pp. 1369–1388, 2004.

41. R. W. Fox and A. T. McDonald, *Introduction to Fluid Mechanics*, John Wiley, New York, 1985.

42. C. T. Crowe, J. N. Chung, and T. R. Troutt, Particle Mixing in Free Shear Flow, *Prog. Energy Combust. Sci.*, vol. 14, pp. 171–194, 1988.

43. W. A. Sirignano, *Fluid Dynamics and Transport of Droplets and Sprays*, chap. 8, Cambridge University Press, New York, 1999.

44. M. Rein, Phenomena of Liquid Drop Impact on Solid and Liquid Surfaces, *Fluid Dyn. Res.*, vol. 12, pp. 61–93, 1993.

45. C. H. R. Mundo, M. Sommerfeld, and C. Tropea, Droplet-Wall Collisions: Experimental Studies of the Deformation and Breakup Process, *Int. J. Multiphase Flow*, vol. 21, pp. 151–173, 1995.

46. C. H. R. Mundo, M. Sommerfeld, and C. Tropea, On the Modeling of Liquid Sprays Impinging on Surfaces, *Atomization and Sprays*, vol. 8, pp. 625–652, 1998.

47. J. T. Houghton et al. (eds.), *Climate Change 2001: The Scientific Basis: Contribution of Working Group I to the 3rd Assessment Report of the Intergovernmental Panel on Climate Change*, Cambridge University Press, New York, 2001.

48. United Nations Environment Programme/World Meteorological Organization, Scientific Assessment of Ozone Depletion: 2002, Global Ozone Research and Monitoring Project Rep. 47, chap. 1, Geneva, Switzerland, 2003.

APPENDIX A

Table A1 Variation of Sauter Mean Diameter (D_{32}), Streamwise (U), and Cross-Stream (V) Mean Velocity Components, and Corresponding Distributions with Radial Position (R) at $Z = -50$ mm for the Unheated and Heated Cylinder (Original Atomizer)

	Unheated Cylinder		
R (mm)	D_{32} (μm)	U (m/s)	V (m/s)
50	—	—	—
40	—	—	—
30	—	—	—
20	33.508	3.777	0.226
10	27.641	4.222	−0.173
0	25.874	4.477	0.322
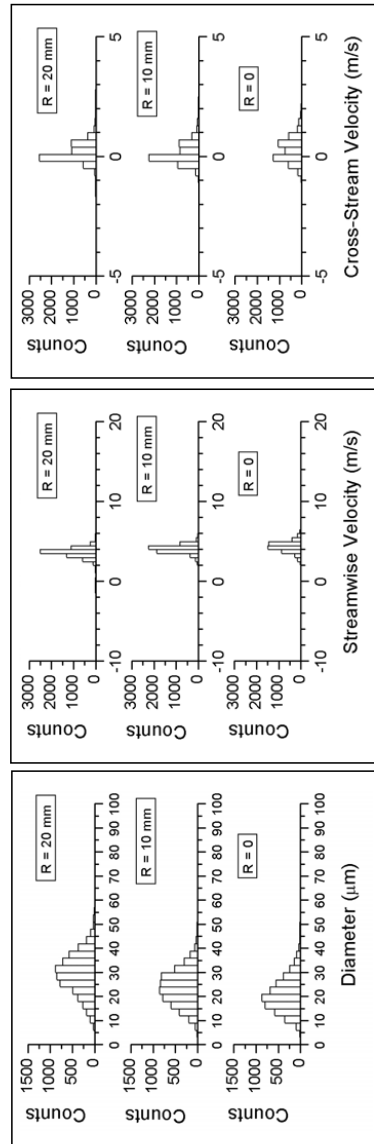
Table A1 (continued)

Heated Cylinder

R (mm)	D_{32} (µm)	U (m/s)	V (m/s)
50	55.632	2.420	0.147
40	48.146	2.985	0.180
30	41.549	3.193	0.159
20	33.588	3.524	0.222
10	28.088	4.032	0.167
0	24.249	3.431	0.243
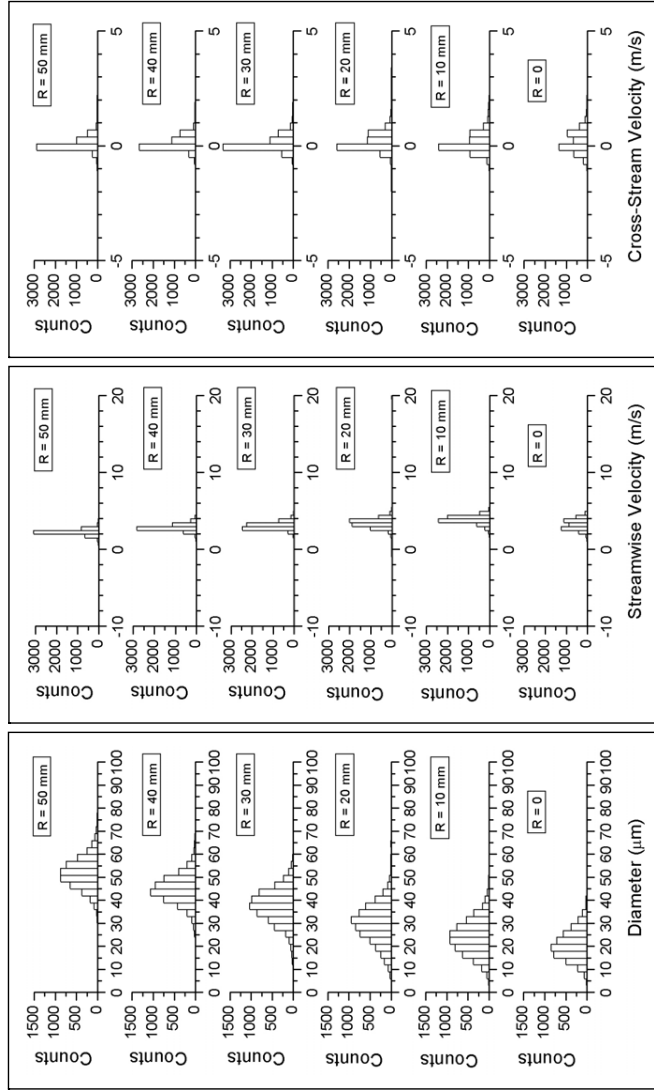
Table A2 Variation of Sauter Mean Diameter (D_{32}), Streamwise (U), and Cross-Stream (V) Mean Velocity Components, and Corresponding Distributions with Radial Position (R) at Z = −50 mm for the Three Agents (replacement atomizer, unheated cylinder)

Water

R (mm)	D_{32} (μm)	U (m/s)	V (m/s)
50	66.398	3.678	0.694
40	58.199	4.581	0.559
30	53.705	8.655	0.619
20	50.134	13.261	0.716
10	47.491	15.024	0.851
0	42.224	8.493	0.689
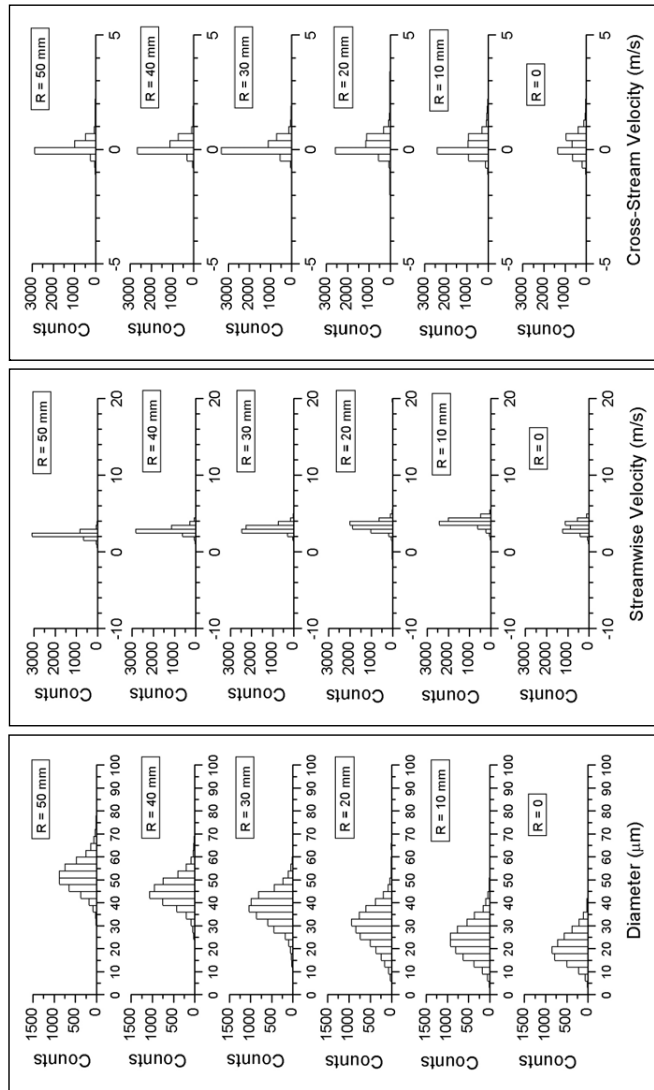
Table A2 (continued)

HFE7100

R (mm)	D_{32} (µm)	U (m/s)	V (m/s)
50	43.679	3.689	0.662
40	37.179	4.623	0.482
30	34.192	9.162	0.378
20	33.247	16.336	0.150
10	32.493	23.248	0.057
0	27.021	16.702	−0.118
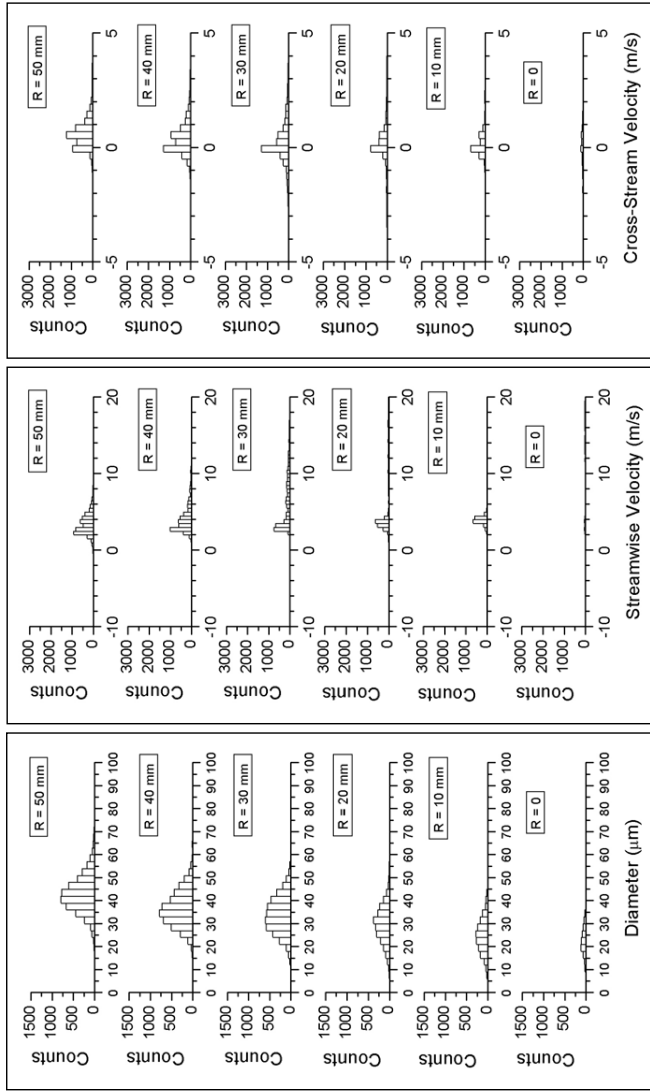
Table A2 (continued)

HFE7000

R (mm)	D_{32} (μm)	U (m/s)	V (m/s)
50	37.868	3.089	0.525
40	32.554	4.241	0.428
30	30.852	10.011	0.341
20	29.426	17.233	-0.113
10	27.371	24.465	-0.460
0	23.996	14.314	0.242
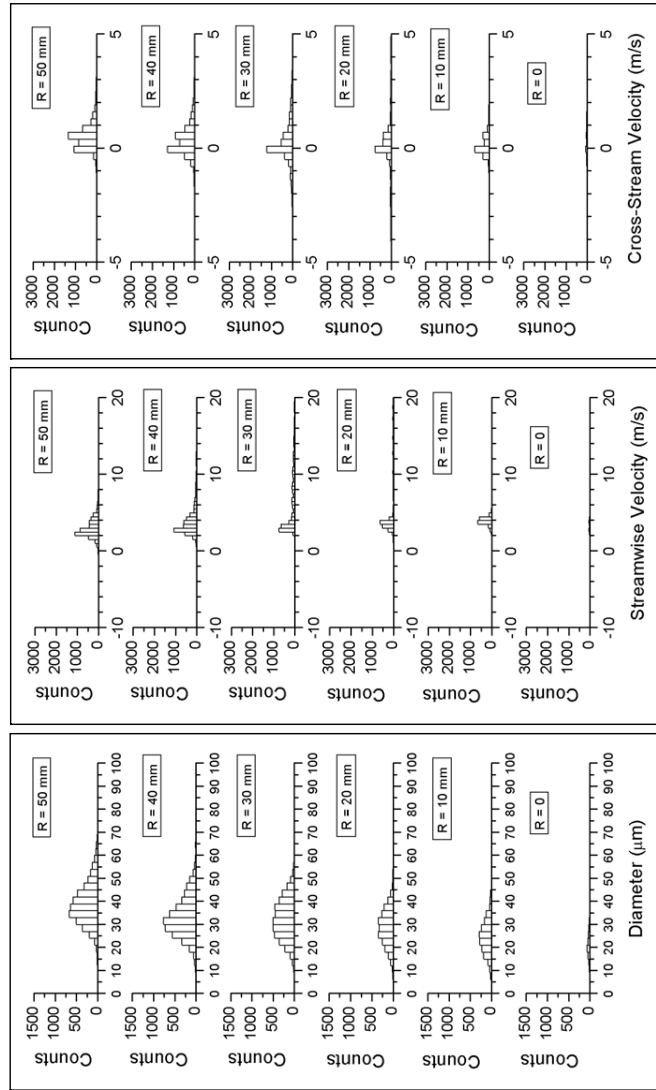
Table A3   Variation of Sauter Mean Diameter (D_{32}), Streamwise (U), and Cross-Stream (V) Mean Velocity Components, and Corresponding Distributions with Radial Position (R) at $Z = -167$ mm (i.e., 20 mm downstream of the atomizer) for the Three Agents (replacement atomizer)

Water

R (mm)	D_{32} (μm)	U (m/s)	V (m/s)
30	68.438	13.202	9.033
25	70.111	16.322	9.435
20	68.085	17.982	8.551
15	62.950	17.228	6.329
10	58.002	17.371	3.997
5	53.618	14.881	0.796
0	53.425	11.985	0.137
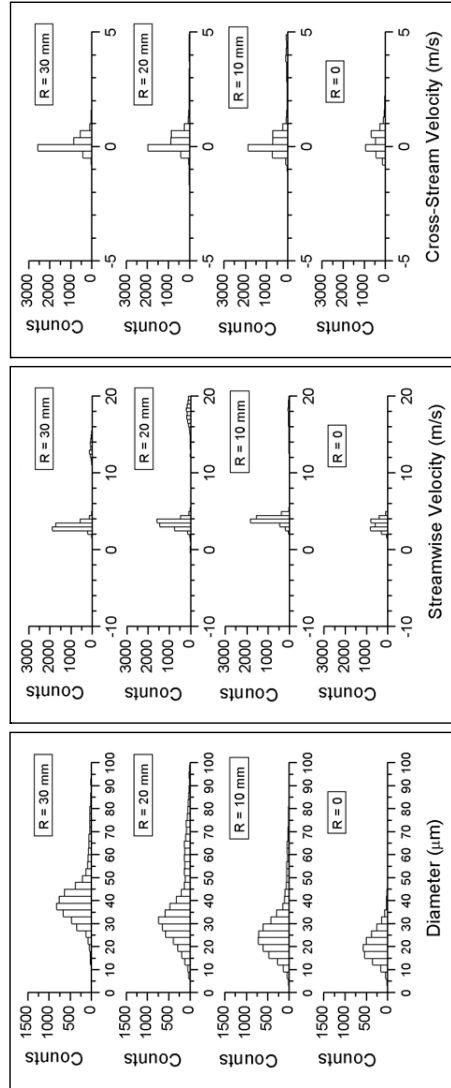
Table A3 (continued)

HFE7100

R (mm)	D_{32} (μm)	U (m/s)	V (m/s)
20	59.067	16.992	8.717
18	59.743	17.618	8.068
17	59.260	18.150	7.794
15	49.899	17.110	6.668

Table A3   (continued)

R (mm)	D_{32} (μm)	U (m/s)	V (m/s)
21	53.130	17.700	9.378
20	56.156	17.901	9.066
18	51.287	17.923	7.642
15	49.391	17.555	5.503

HFE7000